https://doi.org/10.5194/egusphere-2026-2015
Preprint. Discussion started: 21 April 2026


# A comprehensive empirical model for non-linear pressure drag across non-hydrostatic flow regimes with trapped lee waves

Jose Luis Argain [1]

[1]Departamento de Física, FCT, Universidade do Algarve, Campus de Gambelas, 8005-139 Faro, Portugal

**Correspondence:** jargain@ualg.pt

**Abstract.** This study introduces a novel and computationally efficient empirical model to estimate the total pressure drag generated by trapped lee waves and upward-propagating internal waves in moderate to severe non-hydrostatic, stratified flow over a mountain ridge, as a function of flow nonlinearity. The model's core framework is based on a two-layer atmosphere characterised by a piecewise-constant Scorer parameter, $l$. In this configuration, a lower layer extending from the surface to a height $z = H$ is defined by a constant value $l_1$, while an upper layer, extending indefinitely aloft, is characterised by $l_2$, where $l_2 < l_1$. Several features are incorporated into this idealised framework to enable the representation of a wide range of flow regimes over mountainous terrain, including those with realistic vertical profiles of the Scorer parameter. To develop the empirical formulation, a numerical model operating at the micro- to mesoscale is employed. This model is well-suited for simulating realistic, nonlinear flows over high mountains with steep slopes. From idealised cases with simple $l(z)$ profiles to more realistic configurations with complex structures, the empirical model yields results that compare favourably with numerical simulations for flow regimes characterised by moderately to strong nonlinearity. This empirical model serves as a valuable foundation for developing parameterisations within weather prediction models to represent the effects of pressure drag generated in nonlinear flow conditions where trapped lee waves form, alleviating the requirement for high-resolution numerical models to downscale over steep terrain.

**Keywords:** propagating gravity waves; trapped lee waves; resonance; non-hydrostatic effects; linear theory.

## 1 Introduction

Orographic internal gravity waves exert a pressure drag on the topography that generates them. The topography, in turn, applies an equal and opposite force on the atmosphere—a force that can be distributed over considerable vertical and horizontal distances. Parameterising this orographic drag, by specifying its magnitude and spatial distribution, is crucial because numerical weather prediction models lack the resolution to resolve gravity waves generated by small- and medium-scale mountains. These waves significantly decelerate winds throughout the atmosphere and influence the distribution of atmospheric pressure. Without such parameterisation, models remain physically incomplete and produce inaccurate forecasts of the general atmospheric circulation.

Most modern orographic drag parameterisation schemes have been developed for hydrostatic flows, with closed-form expressions for the total drag derived in several foundational studies (Phillips, 1984; Shutts and Gadian, 1999; Smith, 1979a; Teixeira

https://doi.org/10.5194/egusphere-2026-2015
Preprint. Discussion started: 21 April 2026


and Miranda, 2006). The hydrostatic approximation was adopted in many classic studies because mesoscale non-hydrostatic effects are often modest, and this assumption greatly simplifies the analysis.

However, as wind speed increases or static stability decreases, certain aspects of the flow response become distinctly non-hydrostatic. In the hydrostatic regime, all forced wave components propagate vertically. In non-hydrostatic scenarios, high-wavenumber components become evanescent and cease to transport momentum upward, whereas longer waves may continue to propagate and contribute to the drag. If an evanescent layer overlies a propagating layer, strong wave reflection can occur, trapping wave energy. This can lead to resonance and amplified drag, along with partial reflection phenomena that may also emerge even under hydrostatic conditions (Leutbecher, 2001; Teixeira and Miranda, 2005). As demonstrated in studies such as Teixeira et al. 2013a and Teixeira et al. 2013b, the drag generated under non-hydrostatic conditions can be comparable to, or even exceed, its hydrostatic counterpart.

Given that most atmospheric flows over mountains are nonlinear, it is essential to study the impact of nonlinearity on the pressure drag induced by gravity waves. In the hydrostatic regime, this issue has received considerable attention. Lilly and Klemp 1979 solved Long's equation to show how finite amplitude and terrain asymmetry can amplify the wave response and the resulting drag. Smith 1989 reviewed hydrostatic airflow over mountains, proposed scalings for the drag, and clarified the limits of linear theory for different topographic profiles. Durran 1990 synthesised key results for drag in linear hydrostatic flow and discussed how atmospheric structure and finite-amplitude effects modulate it. Olafsson and Bougeault 1996 examined drag enhancement with increasing nonlinearity and the transition to wave breaking in more realistic profiles. Miranda and James 1992 further showed that, for a non-dimensional mountain height $Nh_0/U \sim O(1)$, a wave-breaking regime can develop and substantially enhance drag relative to its linear reference value.

To account for these effects, Smith 1989 proposed an empirical nonlinear correction to linear theory for weak-to-moderately nonlinearity ($Nh_0/U < 0.5$) in stationary hydrostatic flows, noting that linear theory begins to fail significantly as the flow approaches the wave-breaking limit at $Nh_0/U \sim 0.85$. However, these hydrostatic formulations assume free vertical propagation and do not support trapped lee waves (TLW).

In contrast, the behaviour of drag in non-hydrostatic flows under nonlinear conditions has received less attention. Peltier and Clark 1983 simulated 2D and 3D nonlinear mountain waves, documenting amplification regimes, harmonic generation, and transitions to wave breaking. Lott and Teixeira 2016 analysed how the nonlinear intensification of TLW modes and their interaction with critical levels modify the momentum flux and, consequently, the perceived drag as wave amplitude increases. Vosper 2004 demonstrated that, in flows with boundary-layer inversions, linear theory underestimates wave amplitudes when horizontal wavelengths are short relative to the terrain width. It was also shown that large amplitudes can trigger flow separation and rotor formation, implying enhanced drag and significant regime shifts. Doyle et al. (2011), drawing on strongly nonlinear simulations from the T-REX field campaign, reported how wave intensification and breaking, including TLW and rotor patterns, modulate momentum fluxes and drag. Nevertheless, a comprehensive study that explicitly maps drag as a function of nonlinearity in non-hydrostatic flows featuring TLW remains lacking. A recent work by Argain 2026 has verified that nonlinearity effects are comparably important for the drag produced by both upward-propagating waves and TLW.

https://doi.org/10.5194/egusphere-2026-2015
Preprint. Discussion started: 21 April 2026


In Teixeira et al. 2013a, a two-layer atmosphere with piecewise-constant parameters, of the type originally considered by Scorer 1949, is used to evaluate the TLW drag and the drag associated with vertically propagating waves. It is shown that, in some circumstances, TLW drag can be comparable to, or even larger than, the drag due to vertically propagating waves. These results have direct implications for gravity-wave drag parameterisations ((Lott, 1998)). In Teixeira et al. 2013b, the drag associated with lee waves trapped at an inversion capping a neutrally stratified layer is investigated. As in Teixeira et al. 2013a, TLW drag is found to be comparable to the propagating-wave contribution.

The primary motivation for the present work is to develop a practical and easily implementable empirical model that can serve as a viable alternative for parameterising the total pressure drag produced in such flows under nonlinear conditions. The foundational configuration is based on the two-layer model of Scorer 1949, who provided the first convincing theoretical explanation for TLW. In this study, it is demonstrated that the proposed empirical model compares well with numerical simulations for moderately to strongly non-hydrostatic flow regimes with TLW generation under moderate to strong nonlinear conditions.

This article is organised as follows. Section 2 describes the linear model. Section 3 describes the numerical model. Section 4 introduces the empirical model and its theoretical basis. Section 5 presents the model validation, discussion and final remarks on the empirical model. Finally, Section 6 offers concluding remarks.

## 2 Linear model

We consider a linear model for an inviscid, stationary, non-rotating, stratified flow over a 2D mountain ridge of relatively small amplitude, aligned in the $y$ direction. The flow scale is large enough to be treated as approximately inviscid (i.e. an external flow rather than a boundary-layer flow), but small enough for the Earth's rotation to be negligible.

By linearising the equations of motion under the Boussinesq approximation about a reference mean state and expressing the dependent variables as Fourier integrals in $x$, the Fourier transform of the vertical-velocity perturbation, $\widehat{w}$, is shown to satisfy the Taylor–Goldstein equation:

$$\frac{\partial^2 \widehat{w}}{\partial z^2} + \left(l^2 - k^2\right) \widehat{w} = 0, \quad \text{with} \quad l = \left( \frac{N^2}{U^2} - \frac{1}{U} \frac{d^2 U}{dz^2} \right)^{1/2}, \tag{1}$$

where $l$ is the Scorer parameter of the atmosphere. Here, $k$ is the horizontal wavenumber in the $x$ direction, $N^2(z) > 0$ is the static stability of the reference state, and $U(z)$ is the incoming wind speed perpendicular to the ridge. Equation (1) describes how the amplitude of the vertical velocity perturbation for each wavenumber varies with altitude, depending on the vertical structure of the atmosphere through $l(z)$. The existence of TLWs fundamentally requires a vertical decay in the Scorer parameter, $l(z)$, which is a prerequisite for the formation of trapped modes within the lower tropospheric waveguide.

In this model, the atmosphere is divided into vertical layers, each with a constant Scorer parameter. Within each layer, the vertical velocity solution takes a simple mathematical form: either a combination of oscillatory functions (if the flow is propagating) or exponential functions (if it is evanescent), depending on the relationship between the horizontal wavenumber and the local Scorer parameter.

https://doi.org/10.5194/egusphere-2026-2015
Preprint. Discussion started: 21 April 2026


Boundary conditions are imposed to determine the arbitrary constants in each layer. At the surface ($z = 0$), $\widehat{w}$ is determined by the orography ($\widehat{h}(k)$), as the air is forced to rise along the mountain slope. At the interfaces between layers, continuity of vertical velocity and pressure (or its vertical derivative) is required to ensure smooth transitions. Finally, a radiation condition is applied at the top of the uppermost layer to ensure that waves propagate upward or decay without artificial reflection. Once the system is solved for each wavenumber, the complex amplitude $\widehat{w}(k, z)$ is determined for any altitude.

From the linearised horizontal momentum equation, the pressure perturbation $\widehat{p}$ can be expressed in terms of the vertical velocity and its vertical derivative:

$$\widehat{p} = \frac{\rho_0}{ik}\left(U(z)\frac{\partial \widehat{w}}{\partial z} + \widehat{w}\frac{\partial U}{\partial z}\right). \tag{2}$$

Evaluating this expression at $z = 0$ yields the amplitude of the surface pressure perturbation for each wavenumber.

The spatial distribution of the surface pressure, $p(x, z = 0)$, is reconstructed via an inverse Fourier transform. Finally, the pressure drag force across the ridge, per unit length in the span-wise direction, is defined as:

$$D = \int_{-\infty}^{+\infty} p(x, z = 0)\frac{\partial h}{\partial x}dx. \tag{3}$$

The model described above (hereafter DLM – Drag Linear Model) is primarily used to compute resonance modes, $k_{tlw}$, and the total linear pressure drag, $D_L$. Additionally, the linear theoretical models of Teixeira et al. 2013a and Teixeira et al. 2013b are employed. Developed under the same assumptions, these models are applied to idealised atmospheric configurations and allow $D$ to be partitioned into TLW drag ($D_{tlw}$) and vertically propagating wave drag ($D_{pw}$): $D = D_{pw} + D_{tlw}$.

Finally, the orography is assumed to be a symmetric, bell-shaped ridge:

$$h(x) = \frac{h_0}{1 + (x/a)^2} \implies \widehat{h}(k) = \frac{h_0 a}{2}e^{-a|k|}, \tag{4}$$

where $h_0$ is the maximum height and $a$ is the half-width.

## 3 Numerical model

This study employs the FLEX numerical model, a two-dimensional micro-to-mesoscale model formulated in orthogonal curvilinear coordinates. This model has been previously utilised to investigate resonant mountain-wave flows (Argain et al., 2009; Teixeira and Miranda, 2005; Teixeira et al., 2008, 2013a, b).

For any given flow, the horizontal resolution $\Delta x$ is defined as the minimum of $\lambda_{tlw,min}/40$ and $a/5$, where $\lambda_{tlw,min}$ is the smallest calculated wavelength of the TLW. This ensures at least five points per mountain half-width ($a$) and 40 points to represent $\lambda_{tlw,min}$. The vertical grid spacing is set at $\Delta z = 25$ m, providing more than sufficient vertical resolution for all studied cases.

The vertical domain extends to six hydrostatic vertical wavelengths, $\lambda_{z0} = 2\pi/l_1$. The mountain is centred at $x = 0$. The upstream domain length is $15a$, while the downstream domain extends to approximately seven TLW wavelengths, $\lambda_0$, measured

https://doi.org/10.5194/egusphere-2026-2015
Preprint. Discussion started: 21 April 2026


in the linear reference regime. With a model time step of $\Delta t = 1\,\mathrm{s}$, simulations are integrated for approximately $500a/U$ (roughly 14 h).

A sponge layer is applied near the top boundary over a depth of approximately $2.5\,\lambda_{z0}$. At the downstream boundary, the radiation condition of Raymond and Kuo (1984) is imposed. Furthermore, sponge layers spanning 15 and 30 grid points are applied at the upstream and downstream boundaries, respectively.

The FLEX model is calibrated using the $D_L$ values obtained from the DLM. This procedure is essential as the total drag $D$ is highly sensitive to the characteristics of the absorbing sponges at the domain boundaries. The accurate calculation of $D_L$ is vital for the satisfactory performance of the empirical model developed here, as it is used to normalise $D$.

## 4 Empirical model

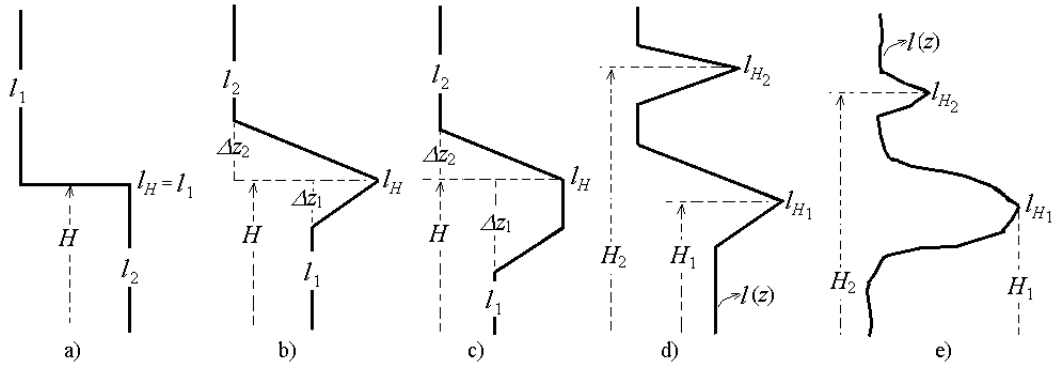


**Figure 1.** Scorer parameter $l(z)$ profiles considered for the development of the empirical model DEM. a) Two-layer Scorer profile. b) Idealised profile with a maximum $l_H$. c) Idealised profile with a maximum $l_H$ at the upper edge of a plateau. d, e) Idealised and arbitrary profiles, respectively, featuring two maxima, $l_{H_1}$ and $l_{H_2}$.

Fig. 1 illustrates the various atmospheric configurations considered for the development of the empirical model. Fig. 1a depicts the two-layer Scorer atmosphere which, as previously noted, forms the basis of this empirical model (hereafter DEM, for Drag Empirical Model). In this baseline configuration, the DLM and FLEX models employ a uniform background wind of $U = 10\,\mathrm{m\,s^{-1}}$. Static stability is prescribed as $N_1 = 0.02\,\mathrm{s^{-1}}$ in the lower layer and $N_2 = 0.004\,\mathrm{s^{-1}}$ in the upper layer, resulting in $N_2/N_1 = 0.2$ and $l_2/l_1 = 0.2$.

For the two-layer Scorer profile (Fig. 1a), the dimensionless mountain height and half-width are determined as $\hat{h}_0 = l_1 h_0$ and $\hat{a} = l_1 a$ (note that the symbol $\hat{}$ should not be confused with $\widehat{}$, which is used for variables in the wavenumber domain, $k$). For more complex profiles, such as those illustrated in Fig. 1b–e, $\hat{h}_0$ and $\hat{a}$ are defined using the maximum value of $l(z)$ closest to the surface that produces TLW. For instance, in the case of the profile in Fig. 1c, $\hat{h}_0 = l_H h_0$ and $\hat{a} = l_H a$, while for Fig. 1d, $\hat{h}_0 = l_{H_1} h_0$ and $\hat{a} = l_{H_1} a$.

https://doi.org/10.5194/egusphere-2026-2015
Preprint. Discussion started: 21 April 2026


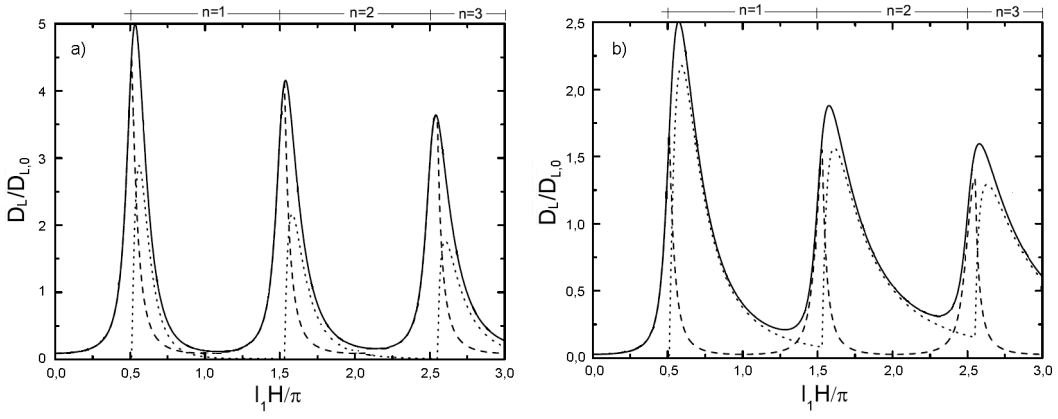


**Figure 2.** Total linear drag $D_L/D_{L,0}$ (solid line) and its decomposition into trapped-wave ($D_{L,tlw}/D_{L,0}$, dotted line) and propagating-wave ($D_{L,pw}/D_{L,0}$, dashed line) contributions, versus dimensionless duct depth $\hat{H} = l_1 H/\pi$, obtained using the theoretical model of Teixeira et al. 2013a. a) $\hat{a} = l_1 a = 2$ (strong non-hydrostatic effect, $a = 1000$ m). b) $\hat{a} = 5$ (moderate non-hydrostatic effect, $a = 2500$ m).

In all studied cases, a bell-shaped mountain profile (4) is employed to facilitate better control over the variation of $a$ and $h_0$. Nonlinearity is varied exclusively through $h_0$, ranging from the linear regime ($\hat{h}_0 = 0.02$) up to $\hat{h}_0 \to 1$ (strongly nonlinear). Larger values of $\hat{h}_0$ are omitted as it was found, following Argain 2026, that in this type of flow, TLW effects on drag variability—the dominant factor in most instances—become secondary for $\hat{h}_0 > 1$. Consistently with Argain 2026, no wave breaking was observed in the cases studied; therefore, the characteristic enhancement of total pressure drag associated with this mechanism is absent.

Figure 2 illustrates the normalised total linear drag $D_L/D_{L,0}$ and its decomposition into linear trapped-wave drag $D_{L,tlw}/D_{L,0}$ and linear propagating-wave drag $D_{L,pw}/D_{L,0}$. These results are presented as a function of the dimensionless duct depth $\hat{H} = l_1 H/\pi$ ($\hat{H} \in [0.5, 3.0]$) and were obtained using the theoretical model of Teixeira et al. 2013a applied to a Scorer atmosphere (Fig. 1a). Here, $D_{L,0} = 0.25\pi\rho_0 l_1 (h_0 U)^2$ is the linear hydrostatic single-layer reference value. Fig. 2a corresponds to $\hat{a} = l_1 a = 2$ (strong non-hydrostatic effect, $a = 1000$ m), while Fig. 2b corresponds to $\hat{a} = 5$ (moderate non-hydrostatic effect, $a = 2500$ m). In both cases, $h_0 = 10$ m, yielding $\hat{h}_0 = l_1 h_0 = 0.02$ (linear regime). As illustrated, in the distinctly non-

https://doi.org/10.5194/egusphere-2026-2015
Preprint. Discussion started: 21 April 2026


hydrostatic regime, $D_{L,tlw}$ can be comparable to, and in some intervals exceed, $D_{L,pw}$, indicating that the TLW contribution may represent a substantial fraction of the total drag.

In Fig. 2b, representing a moderately non-hydrostatic flow, $D_{L,tlw}/D_{L,0}$ is consistently lower than $D_{L,pw}/D_{L,0}$. Nevertheless, $D_{L,tlw}/D_{L,0}$ still accounts for a significant fraction of $D_L/D_{L,0}$ (approximately 50%), in contrast to the classical hydrostatic single-layer reference (see, e.g., Fig. 17a in Teixeira et al. 2013a, where $D_{L,tlw}/D_{L,0}$ is small compared to $D_{L,pw}/D_{L,0}$). Generally, most flows generating TLW, where $D_{L,tlw}$ is comparable to $D_L$, exhibit non-hydrostaticity levels ranging from moderate to severe ($\hat{a} \approx 1-5$). This specific flow regime is the focus of the present study, analysed as a function of nonlinearity. A key insight for the construction of the DEM model, derived from Fig. 2a,b, is the remarkable similarity in the functional form of the drag across different trapped modes. This consistency allows for the definition of a generic drag function, $D(\hat{H})$, initially calibrated for the first mode ($n=1$) within the interval $\hat{H} \in [0.5, 1.5]$. The drag behaviour for higher-order modes ($n>1$) can then be effectively reconstructed by scaling this reference function as a function of $n$.

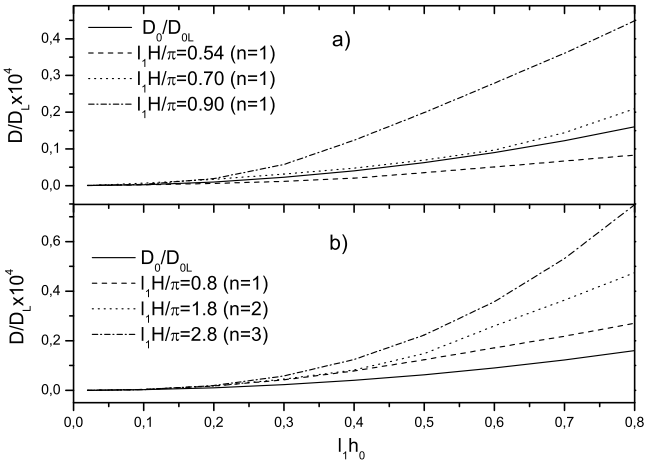


**Figure 3.** Perfis numéricos de $D/D_L(\hat{h}_0)$ para diferentes valores de $\hat{H}$, obtidos com o modelo FLEX. $D_0/D_{L,0}$ is the hydrostatic single layer reference value, normalized by its linear value $D_{L,0}$. a) $\hat{H}=0.8$ ($n=1$ - dash line), $\hat{H}=1.8$ ($n=2$ - dotted line) and $\hat{H}=2.8$ ($n=3$ - dash-dotted line). b) $D/D_L(\hat{h}_0)$ ($n=1$) for $\hat{H}=0.54$ (dash line), $\hat{H}=0.7$ (dotted line) and $\hat{H}=0.9$ (dash-dotted line).

The next step involved conducting a series of numerical simulations with the FLEX model, varying $\hat{h}_0$ within the interval $\hat{h}_0 \in [0.02, 0.8]$ for each value of $\hat{H}$ previously considered in Fig. 2. For instance, Fig. 3a illustrates $D/D_L(\hat{h}_0)$ profiles for $\hat{H}=0.54$, $\hat{H}=0.7$, and $\hat{H}=0.9$ (all falling within the range $\hat{H} \in [0.5, 1.5]$). Fig. 3b presents three analogous profiles: $\hat{H}=0.8$ (mode $n=1$), $\hat{H}=1.8$ (mode $n=2$), and $\hat{H}=2.8$ (mode $n=3$). Here, $D_0/D_{L,0}$ represents the hydrostatic single-layer reference value, normalised by its linear counterpart $D_{L,0}$.

Consistently with Argain 2026, it is observed that for $n=1$ (Fig. 3a), the $D/D_L(\hat{h}_0)$ profiles exhibit a quadratic behaviour ($D/D_L \propto \hat{h}_0^2$), suggesting that the scaling inherited from the linear regime is preserved. This indicates that a function of the form $\Phi\hat{h}_0^2+1$ (where $\Phi$ is a function of $\hat{H}$) can be fitted to these profiles. In Fig. 3b, it is noteworthy that up to $\hat{h}_0 \approx 0.5$ (the moderately nonlinear regime), the profiles for modes $n=1$ and $n=2$ practically coincide; beyond this threshold, the $n=2$ profile diverges, yielding significantly higher drag values. A similar trend occurs between the $n=1$ and $n=3$ profiles, although divergence begins earlier, at approximately $\hat{h}_0 \approx 0.3$. These observations suggest that both the quadratic exponent and the function $\Phi$ must be modified as the mode number $n$ increases.

https://doi.org/10.5194/egusphere-2026-2015
Preprint. Discussion started: 21 April 2026


Based on a detailed analysis of all numerical profiles, the following expression is proposed to estimate $D$ for the two-layer Scorer model (using the $l(z)$ profile shown in Fig. 3a):

$$\frac{D}{D_L}(\overline{H},\overline{h}_0,n) = \left(\Phi(\overline{H})\,\overline{h_0}^2+1\right)\left(\overline{h_0}^{1/4}\,\Psi(\overline{H})\right)^{n-1} \tag{5}$$

where $\overline{h_0} = \hat{h}_0/\hat{h}_{0,1} - 1$ and $\overline{H} = \hat{H}/0.5 - 1$. In this formulation, $\hat{h}_{0,1}$ represents the minimum dimensionless mountain height considered in the numerical simulations. Furthermore, $\hat{H}$ is adjusted such that $\hat{H} = \hat{H} + 0.5$ if $\hat{H} < 0.5$, and $\hat{H} = \hat{H} - \text{nint}(\hat{H}/1.5)$, where nint denotes the nearest integer function. The parameters $D_L$ and $n$ are determined using the DLM model.

The functions $\Phi(\overline{H})$ and $\Psi(\overline{H})$ are defined by the following expressions:

$$\Phi(\overline{H}) = a_1 \exp\left[+a_2\overline{H}^{a_3}\right] + a_4\overline{H}^{a_5} + a_6 \quad \text{for} \quad \hat{H} \le 1.032 \tag{6}$$

$$\Phi(\overline{H}) = b_1 \exp\left[-b_2\overline{H}^{b_3}\right] + b_4\overline{H}^{b_5} + b_6 \quad \text{for} \quad \hat{H} > 1.032 \tag{7}$$

$$\Psi(\overline{H}) = c_1 + \frac{c_2 - c_1}{1+\exp[c_3(\overline{H}-c_4)]} \quad \text{for} \quad \hat{H} \le 0.825 \tag{8}$$

$$\Psi(\overline{H}) = d_2\,\overline{H}^2 + d_1\,\overline{H} + d_0 \quad \text{for} \quad \hat{H} > 0.825 \tag{9}$$

The sets of constants $a_i, b_i, c_i$, and $d_i$, derived from fitting these functions through non-linear optimisation, are as follows:

1. $a_1 = -0.0007272$, $a_2 = 7.0221$, $a_3 = 1.0645$, $a_4 = 4.61$, $a_5 = 2.3724$, and $a_6 = 0.56966$;
2. $b_1 = 2.8863$, $b_2 = 0.031476$, $b_3 = 19$, $b_4 = 0.056042$, $b_5 = -1.1833$, and $b_6 = 2.1822$;
3. $c_1 = 0.642$, $c_2 = 1.0026$, $c_3 = 20.7235$, and $c_4 = 0.29845$;
4. $d_2 = -2.31083$, $d_1 = 0.76594$, and $d_0 = 1.748$.

These functions are specifically designed to capture the regime transitions and the modal dependence inherent in the moderate to severe non-hydrostatic flow. By distinguishing between different ranges of the dimensionless duct depth $\hat{H}$, the model accounts for the shifting dominance of trapped lee wave modes. Furthermore, the high precision of the reported constants is essential for the numerical reproducibility of the DEM, ensuring consistent drag estimations across the diverse atmospheric configurations explored in this study.

The maximum number of modes considered in this study is restricted to $n = 3$, as atmospheric configurations exceeding this threshold are rare in nature. Furthermore, incorporating higher-order modes would significantly increase the model's complexity without a proportional gain in practical applicability. It is also noteworthy that numerical simulations demonstrate that as $n$

https://doi.org/10.5194/egusphere-2026-2015
Preprint. Discussion started: 21 April 2026


increases, achieving a quasi-stationary state for the drag $D$ becomes increasingly challenging, requiring higher computational stability to ensure convergence.

When the Scorer parameter profile $l(z)$ exhibits multiple maxima ($l_H$) capable of generating trapped lee waves (TLW), such as the configurations shown in Figs. 1d and 1e, the total surface drag $D(\hat{h}_0)$ must account for the collective contribution of these features. Accordingly, based on Eq. (5), the drag is calculated as follows:

$$\frac{D}{D_L}(\overline{h}_0) = \frac{1}{D_L}\sum_{i=1}^{m} D_i(\overline{H}_i, \overline{h}_0, n_i), \tag{10}$$

where $m$ is the number of maxima generating TLW and $n_i$ denotes the number of modes associated with each maximum $\overline{H}_i$. It is important to note that determining $m$ requires identifying, through the DLM, which maxima effectively contribute to TLW by a process of exclusion. Equation (10) constitutes the final formulation of the Drag Empirical Model (DEM) proposed herein.

A key feature of the DEM is the normalisation of the drag profiles by $D_L$. Beyond ensuring that $D/D_L$ equals unity in the linear regime, this approach allows the model to be applied to flows with more complex $l(z)$ structures and enables, for instance, the uniformisation of flows, with distinct $l(z)$ profiles. For each Scorer $l(z)$ profile (Fig. 1a) corresponding to a specific $\hat{H}$, profiles of the types shown in Figs. 1b–d (maintaining the same $\hat{H}$) were idealised. A comparison of the simulated $D/D_L(\hat{h}_0)$ profiles across these four cases (Figs. 1a–d) revealed that, for a given value of $\hat{H}$, the profiles are remarkably similar and, in some instances, practically coincident.

Figure 4a compares two non-normalized $D(\hat{h}_0)$ profiles sharing the same value of $\hat{H}$, highlighting how different $l(z)$ structures influence the drag. One profile corresponds to the standard Scorer atmosphere (solid lines, Fig. 1a), while the other represents an alternative configuration. Specifically, lines without symbols denote $\hat{H} = 0.6$, and those with symbols indicate $\hat{H} = 1.07$. For the $\hat{H} = 0.6$ case, the dotted line represents an extreme configuration similar to that investigated by Teixeira et al. 2013b, where lee waves are trapped by a very thin inversion capping a neutrally stratified layer ($l_1 = 0$,m$^{-1}$, as shown in Fig. 1b). In this instance, the inversion at $H = 500$ m (with $l_H = 1.25 \times 10^{-3}$ m$^{-1}$) is characterized by parameters $\Delta z_1 = \Delta z_2 = 25$ m, with $l_2 = 1 \times 10^{-3}$ m$^{-1}$ above. As illustrated, the profiles for the Scorer case (solid line) and the thin inversion case (dotted line) diverge significantly despite their identical $\hat{H}$ values.

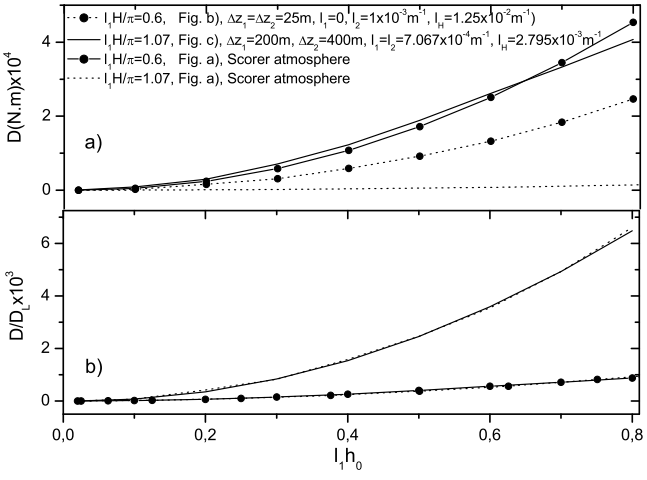


**Figure 4.** a) Comparação entre dois perfis de $D(\hat{h}_0)$ (não normalizados com $D_L$) com o mesmo valor de $\hat{H}$. b) Como em a) mas com os perfis $D(\hat{h}_0)$ normalizados, i.e., $D/D_L(\hat{h}_0)$.

For $\hat{H} = 1.07$, the dotted line with symbols corresponds to an $l(z)$ profile of the type shown in Fig. 1c with the following parameters: $H = 1000$ m, $l_H = 2.8 \times 10^{-3}$ m$^{-1}$, $l_1 = 1.4 \times 10^{-3}$ m$^{-1}$, $l_2 = 2.8 \times 10^{-4}$ m$^{-1}$, $\Delta z_1 = 200$ m, and $\Delta z_2 = 400$ m.

https://doi.org/10.5194/egusphere-2026-2015
Preprint. Discussion started: 21 April 2026


The solid line with symbols represents the baseline Scorer profile. A comparison of these two $D(\hat{h}_0)$ profiles reveals that, consistent with the previous case, they differ considerably.

Maintaining the same symbology, Fig. 4b presents the same profiles as Fig. 4a, but normalised by their corresponding linear values, i.e., $D/D_L(\hat{h}_0)$. A high degree of coincidence is observed between the profiles for both $\hat{H} = 0.6$ and $\hat{H} = 1.07$. Consequently, it is evident that normalising by $D_L$ for flows with different $l(z)$ profiles but identical $\hat{H}$ values enables the two-layer Scorer model to serve as the baseline for the DEM.

It is worth noting that in regions characterized by abrupt transitions in the linear drag $D_L/D_{L,0}$ between modes (see Fig. 2), numerical simulations of $D$ presented significant challenges, even in moderately non-linear regimes. Achieving a stable temporal evolution required higher spatial and temporal resolutions, along with considerably longer integration times to ensure convergence. This suggests that the linear physics in these regions is nearly singular. While the DEM 'smooths' these transitions—potentially masking extreme resonance behaviors that occur in nature—these abrupt transition zones are relatively narrow. Consequently, they have a minor impact on the overall applicability and robustness of the model.

## 5 Model validation and discussion

Next, we briefly describe a set of observational TLW data that serves as a valuable real-world benchmark for validating the performance of the proposed empirical model. This validation involves comparing observed profiles with numerical results (obtained from the FLEX model) for $D/D_L(\hat{h}_0)$. For simplicity and to facilitate the variation of $\hat{h}_0$, a bell-shaped mountain profile (4) is adopted rather than the actual orography associated with the observations. The observational profiles are displayed in Fig. 5, and the parameters derived from applying the DLM model to these profiles are provided in Table 1.

Sachsperger et al. 2015 presented a numerical analysis of lee waves trapped at the atmospheric boundary-layer inversion, where the vertical $l(z)$ profile exhibits distinct stability regimes that govern wave trapping and propagation. Applying the DLM model to this $l(z)$ profile reveals a single $l_H$ maximum and one associated mode ($n = 1, m = 1$).

Chan 2007 presented an observational case over Hong Kong, where a vertical $l(z)$ profile was derived from wind profiler and radiometer data. This profile is consistent with stationary lee waves downstream of a valley on Lantau Island, exhibiting a wavelength of approximately 2.8 km. Applying the DLM to this profile reveals a single $l_H$ maximum associated with two TLW modes ($m = 1, n = 2$), rather than the single mode suggested by the author.

Smith 1976 reported aircraft-based observations of lee waves over the Blue Ridge Mountains, revealing vertical velocities and wave amplitudes under strong westerly flow. The observed horizontal wavelengths evidenced vertical trapping, attributed to an $l(z)$ profile decaying aloft due to reduced static stability in the free troposphere. Similar to Sachsperger et al. 2015, this case is characterised by $m = 1$ and $n = 1$.

https://doi.org/10.5194/egusphere-2026-2015
Preprint. Discussion started: 21 April 2026


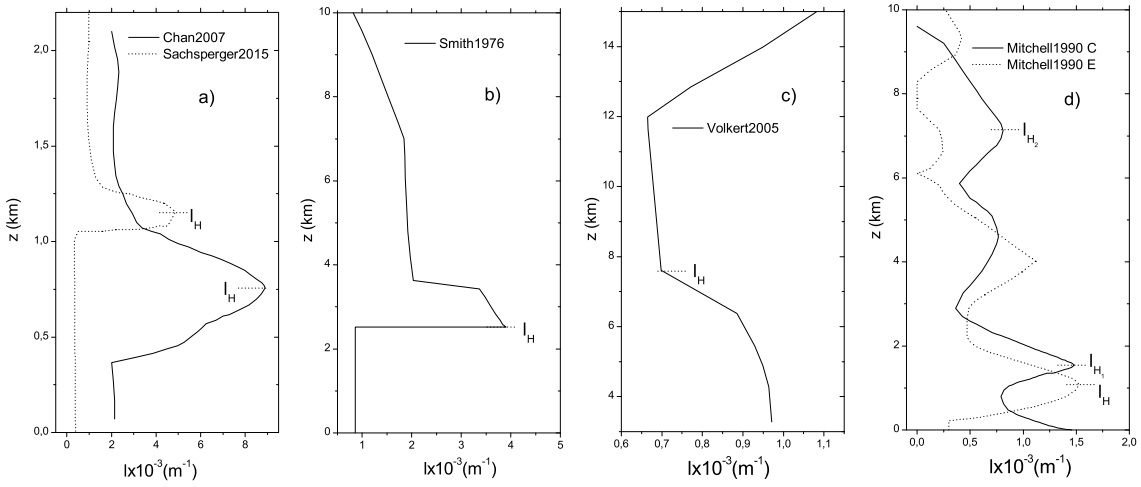


**Figure 5.** Perfis observacionais usados para testar o presente modelo empírico, DEM. a) Sachsperger et al. 2015 (dotte line), Chan 2007 (solid line). b) Smith 1976. c) Volkert et al. 2005. d) Mitchell et al. 1990, perfil $C$ - solid line e perfil $E$ - dotted line.

Volkert et al. 2005 presented a phase diagram distinguishing between TLW and vertically propagating mountain waves based on the $\ell(z)$ profile. This schematic depicts phase lines for a profile with upper-level evanescence, where $l(z)$ decays sufficiently to favour horizontal wave trapping over vertical propagation. As with Chan 2007, the DLM reveals two TLW modes associated with a single $l(z)$ maximum ($m = 1, n = 2$).

Finally, Mitchell et al. 1990 presented satellite observations of Macquarie Island, revealing pronounced cloud bands associated with TLW generated by the island's orography. These features exhibited transverse crests perpendicular to the prevailing wind, consistent with stationary waves under local stability and vertical shear. From this study, we utilise observational $l(z)$ profiles $C$ and $E$. Profile $C$ exhibits two $l(z)$ maxima, each with one associated mode ($m = 2, n_1 = 1, n_2 = 1$), while sounding $E$ reveals a single maximum with one mode ($m = 1, n = 1$). Notably, both profiles contain a local maximum that does not produce TLW: $l(z) = 7.7 \times 10^{-4}\,\mathrm{m}^{-1}$ at $z \approx 4600\,\mathrm{m}$ for profile $C$, and $l(z) = 1.1 \times 10^{-3}\,\mathrm{m}^{-1}$ at $z \approx 4000\,\mathrm{m}$ for profile $E$.

https://doi.org/10.5194/egusphere-2026-2015
Preprint. Discussion started: 21 April 2026


| **Observations (Fig. 5)** | **Parameters (DLM model)** |
|---|---|
| Sachsperger et al. 2015 | $m = 1$, $n = 1$, $\lambda_{tlw} = 4974\,\text{m}$, $l_H = 4.87 \times 10^{-3}\,\text{m}^{-1}$, $H = 1153\,\text{m}$, $\hat{H} = 1.79$, $a = 1000\,\text{m}$ $\hat{a} = 4.9$ (moderate non-hydrostatic effects |
| Chan 2007 | $m = 1$, $n = 2$, $\lambda_{tlw1} = 2740\,\text{m}$, $\lambda_{tlw2} = 942\,\text{m}$, $l_H = 8.9 \times 10^{-3}\,\text{m}^{-1}$, $H = 750\,\text{m}$, $\hat{H} = 2.12$, $a = 450\,\text{m}$ $\hat{a} = 4$ (moderate non-hydrostatic effects) |
| Smith 1976 | $m = 1$, $m = 1$, $\lambda_{tlw} = 7450\,\text{m}$, $l_H = 3.9 \times 10^{-3}\,\text{m}^{-1}$,$H = 2520\,\text{m}$, $\hat{H} = 3.13$, $a = 1000\,\text{m}$, $\hat{a} = 3.9$ (moderate non-hydrostatic effects) |
| Volkert et al. 2005 | $m = 1$, $n = 2$, $l_H = 7 \times 10^{-4}\,\text{m}^{-1}$, $\lambda_{tlw,1} = 14615\,\text{m}$ e $\lambda_{tlw,2} = 8820\,\text{m}$, $H = 7609\,\text{m}$, $\hat{H} = 1.69$, $a = 2000\,\text{m}$, $\hat{a} = 1.4$ (strong non-hydrostatic effects) |
| Mitchell et al. 1990 $C$ | $m = 2$, $n_1 = 1$, $n_2 = 1$, $l_{H_1} = 1.47 \times 10^{-3}\,\text{m}^{-1}$, $\lambda_{tlw,1} = 8920\,\text{m}$, $H_1 = 1536\,\text{m}$, $\hat{H}_1 = 0.72$ $l_{H_2} = 7.93 \times 10^{-4}\,\text{m}^{-1}$, $\lambda_{tlw,2} = 13250\,\text{m}$ $H_2 = 7104\,\text{m}$, $\hat{H}_2 = 1.79$, $a = 2000\,\text{m}$, $\hat{a} = l_{H_1} a = 2.94$ (moderate non-hydrostatic effects) |
| Mitchell et al. 1990 $E$ | $m = 1$, $n = 1$, $l_H = 1.52 \times 10^{-3}\,\text{m}^{-1}$, $\lambda_{tlw} = 8650$, $H = 1095\,\text{m}$, $\hat{H} = 0.53$, $a = 1000\,\text{m}$, $\hat{a} = 1.5$ (strong non-hydrostatic effects) |

**Table 1.** Parâmetros obtidos com o modelo DLM para os perfis de $l(z)$ resultantes de observações.

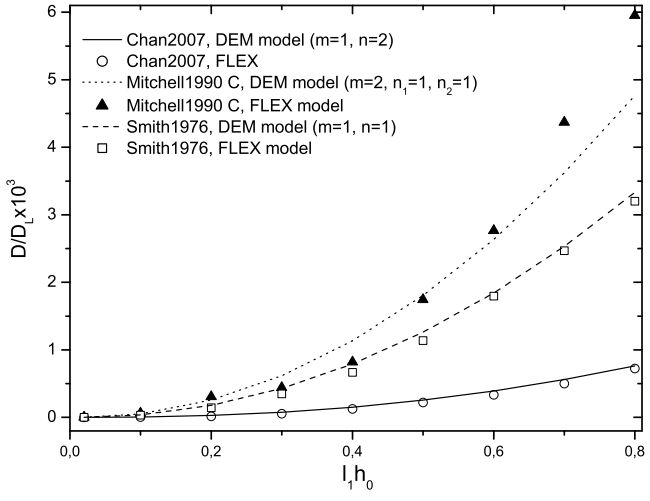


**Figure 6.** $D/D_L(\hat{h}_0)$ profiles obtained using the FLEX and DEM models for the observational $l(z)$ profiles reported by Chan 2007, Smith 1976, and Mitchell et al. 1990 $C$.

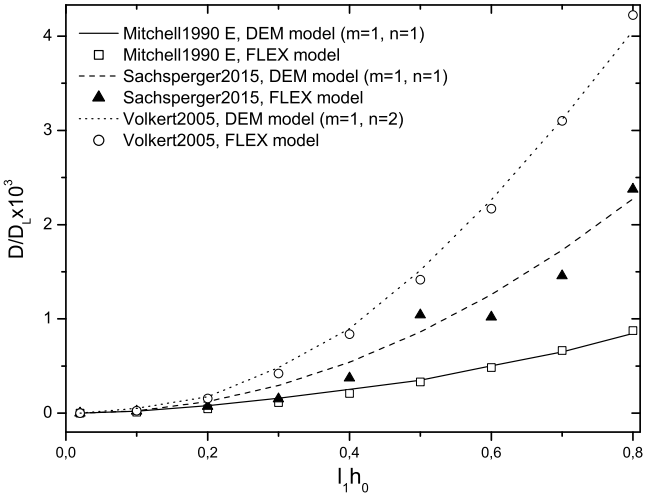


**Figure 7.** As in Fig. 6 but for the observational $l(z)$ profiles from Sachsperger et al. 2015, Volkert et al. 2005, and Mitchell et al. 1990 $E$.

Figures 6 and 7 present the $D/D_L(\hat{h}_0)$ profiles obtained using the FLEX and DEM models for each of the aforementioned observational $l(z)$ profiles. With the exception of Sachsperger et al. 2015 and the Mitchell et al. 1990 $C$ case, applying both

https://doi.org/10.5194/egusphere-2026-2015
Preprint. Discussion started: 21 April 2026


models to the observational profiles yielded highly consistent $D/D_L(\hat{h}_0)$ results. The Mitchell et al. 1990 $C$ case is the most complex, featuring two maxima, each with an associated TLW mode ($m = 2, n_1 = 1, n_2 = 1$). In this instance, the greatest discrepancies occur in the strongly non-linear regime ($\hat{h}_0 > 0.7$). Nonetheless, the overall agreement between the $D/D_L(\hat{h}_0)$ profiles remains robust. Regarding the Sachsperger et al. 2015 case, the numerical profile exhibits significant scatter compared to the other simulations, making it difficult to definitively validate the DEM performance for this specific instance. However, it is noteworthy that the DEM profile appears to follow the general trend of these scattered points. Overall, these results demonstrate that the DEM performs remarkably well across a range of atmospheric conditions.

### Final remarks on the DEM

The 2D flow considered in the development of the Drag Empirical Model (DEM) is assumed to be of a sufficiently large scale to be considered approximately inviscid—characterised here as an "external" flow—while remaining small enough for the Earth's rotation to be neglected. In this context, "external flow" refers to a configuration where the boundary layer (BL) is either negligible or the flow of interest lies above the region dominated by surface friction and separation.

In the real atmosphere, the BL typically spans from a few hundred metres to approximately 1 km. Above this depth, the flow is effectively inviscid and can be accurately described using free-slip conditions. Consequently, adopting an inviscid, free-slip lower boundary is physically consistent for many practical scenarios where the BL is thin and its influence on wave generation is secondary.

As reported in Argain 2026, the evolution of the wave field with increasing $\hat{h}_0$ indicates that this non-hydrostatic, inviscid configuration precludes both wave breaking and classical rotors. These phenomena are intrinsically linked to friction and flow separation (no-slip conditions), which are not represented in the present numerical framework. In the absence of rotors, the system responds primarily through internal wave mechanisms: duct resonance detuning, harmonic generation, spatial reorganisation, and leakage into propagating waves. These processes typically lead to drag saturation or redistribution rather than a sharp monotonic increase.

Nevertheless, since trapped lee waves (TLW) and rotors are frequently interconnected, neglecting boundary-layer friction removes a vital dissipation mechanism that would otherwise limit wave amplitude. It is therefore recognised that, by suppressing friction, the DEM may provide a theoretical upper limit that overestimates drag in specific rotor-prone regimes. Despite these limitations, the results demonstrate that the DEM remains a robust and applicable tool for a wide range of realistic atmospheric scenarios.

## 6 Conclusions

This study introduces and validates the Drag Empirical Model (DEM), a novel framework for calculating total pressure drag in moderate to severe non-hydrostatic flows characterised by trapped lee waves (TLW). By adopting a two-layer Scorer at-

https://doi.org/10.5194/egusphere-2026-2015
Preprint. Discussion started: 21 April 2026


mosphere as a fundamental baseline, the model offers a computationally inexpensive alternative to high-resolution numerical simulations.

- The normalisation of total drag by its linear counterpart ($D_L$) serves as a robust unifying framework. This approach allows the complex dependence of drag on the Scorer parameter structure to be collapsed into a nearly universal set of non-linear correction functions, irrespective of the specific vertical profile of $l(z)$.
- Non-linear drag enhancement in the presence of TLW is critically dependent on the mode number $n$. While the fundamental mode ($n = 1$) largely maintains the quadratic scaling characteristic of linear theory, higher-order modes exhibit marked divergence as nonlinearity increases. The DEM successfully accounts for this behaviour through its mode-dependent formulation.
- The model demonstrates consistent accuracy when validated against numerical simulations (FLEX) across a diverse range of realistic atmospheric soundings, from idealised configurations to complex observational cases.

By capturing the essential physics of resonance and non-linear saturation, the DEM establishes a viable pathway for improving orographic drag parameterisations in operational weather and climate models. Its implementation could significantly reduce the computational overhead required to resolve non-hydrostatic effects over steep terrain. Future research should focus on incorporating surface friction and three-dimensional topographic effects to further extend the applicability and realism of this empirical framework.

https://doi.org/10.5194/egusphere-2026-2015
Preprint. Discussion started: 21 April 2026


## References

Argain, J. L.: Pressure drag produced by trapped lee waves and propagating mountain waves under nonlinear conditions, EGUsphere, 2026.

Argain, J. L., Miranda, P. M. A., and Teixeira, M. A. C.: Estimation of the friction velocity in stably stratified boundary layer flows over hills, Boundary-Layer Meteorol., 130, 15–28, 2009.

Chan, P. W.: Atmospheric Waves Associated with a Valley of Lantau Island: Observation, Theory and Numerical Simulation, 12th Conference on Mesoscale Processes, American Meteorological Society, Waterville Valley, NH, USA, 2007.

Doyle, J. D. and Coauthors: An intercomparison of T-REX mountain-wave simulations and implications for mesoscale predictability, Mon. Weather Rev., 139, 2811–2831, 2011.

Durran, D. R.: Mountain Waves and Downslope Winds, in: Atmospheric Processes over Complex Terrain, Meteorological Monographs, Vol. 23, American Meteorological Society, Boston, MA, 59–81, 1990.

Gill, A. E.: Atmosphere-Ocean Dynamics, Academic Press, San Diego, CA, 1982.

Leutbecher, M.: Surface pressure drag for hydrostatic two-layer flow over axisymmetric mountains, J. Atmos. Sci., 58, 797–807, 2001.

Lilly, D. K. and Klemp, J. B.: The effects of terrain shape on nonlinear hydrostatic mountain waves, J. Fluid Mech., 95, 241–261, 1979.

Long, R. R. and Chimakurti, G.: Numerical Model for Nonlinear Hydrostatic Flow over Orography, J. Atmos. Sci., 69, 2558–2575, 2012.

Lott, F.: A study of the low frequency inertio-gravity waves observed during PYREX, J. Geophys. Res., 103, 1747–1757, 1998.

Lott, F. and Teixeira, M. A. C.: A new theory for downslope windstorms and trapped mountain waves, J. Atmos. Sci., 73, 3585–3597, 2016.

McFarlane, N. A.: The effect of orographically excited gravity-wave drag on the general circulation of the lower stratosphere and troposphere, J. Atmos. Sci., 44, 1775–1800, 1987.

Miranda, P. M. A. and James, I. N.: Non-linear three-dimensional effects on gravity-wave drag: splitting flow and breaking waves, Q. J. Roy. Meteor. Soc., 118, 1057–1081, 1992.

Mitchell, R. M., Cechet, R. P., Turner, P. J., and Elsum, C. C.: Observation and Interpretation of Wave Clouds over Macquarie Island, Q. J. Roy. Meteor. Soc., 116, 741–752, 1990.

Olafsson, H. and Bougeault, P.: Nonlinear flow past an elliptic mountain ridge, J. Atmos. Sci., 53, 2465–2489, 1996.

Peltier, W. R. and Clark, T. L.: Nonlinear mountain waves in two and three spatial dimensions, Q. J. Roy. Meteor. Soc., 109, 527–548, 1983.

Phillips, D. S.: Analytical surface pressure and drag for linear hydrostatic flow over three-dimensional elliptical mountains, J. Atmos. Sci., 41, 1073–1084, 1984.

Sachsperger, J., Serafin, S., and Grubišić, V.: Lee Waves on the Boundary-Layer Inversion: Their Dependence on Atmospheric Stability, Front. Earth Sci., 3, 70, 2015.

Sawyer, J. S.: Numerical calculation of the displacements of a stratified airstream crossing a ridge of small height, Q. J. Roy. Meteor. Soc., 86, 326–345, 1960.

Scorer, R. S.: Theory of waves in the lee of mountains, Q. J. Roy. Meteor. Soc., 75, 41–56, 1949.

Shutts, G. J. and Gadian, A.: Numerical simulations of orographic gravity waves in flows which back with height, Q. J. Roy. Meteor. Soc., 125, 2743–2765, 1999.

Smith, R. B.: The Generation of Lee Waves by the Blue Ridge, J. Atmos. Sci., 33, 2548–2560, 1976.

Smith, R. B.: The influence of mountains on the atmosphere, Adv. Geophys., 21, 87–230, 1979.

Smith, R. B.: The Influence of Mountains that Cause Partial Wave Breaking on the Flow near the Ground, Tellus, 31, 351–359, 1979.

Smith, R. B.: Hydrostatic airflow over mountains, Adv. Geophys., 31, 1–41, 1989.

https://doi.org/10.5194/egusphere-2026-2015
Preprint. Discussion started: 21 April 2026


Stensrud, D. J.: Parametrization Schemes: Keys to Understanding Numerical Weather Prediction Models, Cambridge University Press, Cambridge, UK, 2009.

Teixeira, M. A. C. and Miranda, P. M. A.: Linear criteria for gravity-wave breaking in resonant stratified flow over a ridge, Q. J. Roy. Meteor. Soc., 131, 1815–1820, 2005.

Teixeira, M. A. C. and Miranda, P. M. A.: A linear model of gravity wave drag for hydrostatic sheared flow over elliptical mountains, Q. J. Roy. Meteor. Soc., 132, 2439–2458, 2006.

Teixeira, M. A. C., Miranda, P. M. A., and Argain, J. L.: Mountain waves in two-layer sheared flows: critical level effects, wave reflection, and drag enhancement, J. Atmos. Sci., 65, 1912–1926, 2008.

Teixeira, M. A. C., Argain, J. L., and Miranda, P. M. A.: Drag produced by trapped lee waves and propagating mountain waves in a two-layer atmosphere, Q. J. Roy. Meteor. Soc., 139, 964–981, 2013.

Teixeira, M. A. C., Argain, J. L., and Miranda, P. M. A.: Orographic drag associated with lee waves trapped at an inversion, J. Atmos. Sci., 70, 2930–2947, 2013.

Volkert, H. and EUMETRAIN/DLR collaborators: Physical Background of Lee Waves: Trapped versus Vertically Propagating, in: EUMETRAIN Training Modules, EUMETRAIN/DLR, 2005.

Vosper, S. B.: Inversion effects on mountain lee waves, Q. J. Roy. Meteor. Soc., 130, 1723–1748, 2004.

*Acknowledgements.* The author acknowledges the assistance of the Gemini AI model (Google) in language editing .
The author acknowledges the assistance of the Gemini AI model (Google) in language editing

*Competing interests.* The author declares that no competing interests are present.